Post-subdution evolution of the Northern Lhasa Terrane, Tibet: Constraints from geochemical anomalies, chronology and petrogeochemistry

Shi-mian Yu, Xu-dong Ma, Yan-chun Hu, Wei Chen, Qing-ping Liu, Yang Song, Ju-xing Tang

Citation: Shi-mian Yu, Xu-dong Ma, Yan-chun Hu, Wei Chen, Qing-ping Liu, Yang Song, Ju-xing Tang, 2022. Post-subdution evolution of the Northern Lhasa Terrane, Tibet: Constraints from geochemical anomalies, chronology and petrogeochemistry, China Geology, 5, 84-95. doi: 10.31035/cg2021045.

View online: https://doi.org/10.31035/cg2021045

China Geology 5 (2022) 84–95

China Geology

Journal homepage: http://chinageology.cgs.cn
https://www.sciencedirect.com/journal/china-geology

Post-subdution evolution of the Northern Lhasa Terrane, Tibet: Constraints from geochemical anomalies, chronology and petrogeochemistry

Shi-mian Yu[a, b,*], Xu-dong Ma[b,*], Yan-chun Hu[c], Wei Chen[b], Qing-ping Liu[b], Yang Song[b], Ju-xing Tang[b]

[a] *Geological Museum of Guizhou*, *Guiyang* 550081, *China*
[b] *MNR Key Laboratory of Metallogeny and Mineral Assessment*, *Institute of Mineral Resources*, *Chinese Academy of Geological Sciences*, *Beijing* 100037, *China*
[c] *No.*1 *Institute of Geology and Mineral Resources of Shandong Province*, *Jinan* 250014, *China*

ARTICLE INFO

Article history:
Received 11 May 2021
Received in revised form 3 July 2021
Accepted 15 August 2021
Available online 26 August 2021

Keywords:
Bangong-Nujiang collisional zone
Geochemical anomalies
Mineralization
Slab rolling-back/break-off
Delamination
Northern Lhasa Terrane
Geological survey engineering
Tibet

ABSTRACT

Bangong-Nujiang collisional zone (BNCZ) is an older one in Qinghai-Tibet Plateau and resulted in the famous Bangong-Nujiang metallogenic belt, which plays an important role in evaluating the formation and uplift mechanism of plateau. The northern and central Lhasa Terrane composed the southern part of the BNCZ. Since ore deposits can be used as markers of geodynamic evolution, the authors carried 1∶50000 stream sedimental geochemical exploration in the Xiongmei area in the Northern Lhasa Terrane to manifest the mineralization, and based on this mineralization with geochemical and chronological characteristics of related magmatic rocks to constrain their geodynamics and connection with the evolution of the Lhasa Terrane. The authors find Early Cretaceous magma mainly resulted in Cu, Mo mineralization, Late Cretaceous magma mainly resulted in Cu, Mo, and W mineralization in the studying area. The results suggest a southward subduction, slab rolling back and break-off, and thickened lithosphere delamination successively occurred within the Northern Lhasa Terrane.

1. Introduction

Qinghai-Tibet Plateau is a prominent continent-continent collisional zone, where a series of W-E trending blocks collided and amalgamated along several sutures (Fig. 1; Yin A and Harrison TM, 2000). Among these collisional zones, Bangong-Nujiang collisional zone (BNCZ) is an older one and resulted in the famous Bangong-Nujiang metallogenic belt (Li GM et al., 2017; Li XK et al., 2018b). BNCZ plays an important role in evaluating the formation and uplift mechanism of Tibetan Plateau (Zhu DC et al., 2016; Zhao ZB et al., 2021). Northern and Central Lhasa Terrane composed the southern part of the BNCZ, they experienced the evolution from subduction, collision to intracontinental (Fig. 1b). Several models were proposed for the complex geological processes in Northern and Central Lhasa Terrane, involving southward or northward subduction during subduction (Zhu DC et al., 2009, 2011, 2013; Kapp P and DeCelles PG, 2019; Liu YM et al., 2017), slab rolling back and/or sequential break-off during Lhasa-Qiangtang collision (Zhu DC et al., 2011, 2016; Chen Y et al., 2014; Li XK et al., 2018b; Wang Y et al., 2019a), and lithospheric delamination after crustal thickening (Hu PY et al., 2017; Sun M et al., 2020) and some details in these geological processes. These arguments complicate the evolution of the BNCZ, which resulted in the details of evolution in this collisional zone are ongoing debated (Zhu DC et al., 2009, 2011, 2016).

Since deposits always formed in a specific tectonic setting, ore deposits can be used as markers of geodynamic evolution (Mao JW et al., 2021). One of the classic examples is the Central Andes, where Cenozoic porphyry copper deposits in Chile are representative of an active continental margin setting, and the Bolivian tin belt is indicative of a back-arc setting. Both metal belts formed in specific and relatively narrow time windows at 10 Ma scale, which was modulated by periods of flat-slab subduction (James DE and Sacks IS, 1999; Kay SM et al., 1999; Lehmann B, 2004). One more similar example is the southeast China coast, where a Middle to Late Jurassic magmatic arc associated with a ca. 171–153 Ma porphyry copper belt, coupled with the 165–150

* Corresponding author: *E-mail address*: 2644775407@qq.com (Shi-mian Yu); maxudong2011@126.com (Xu-dong Ma).

Literary editor: Xi-jie Chen
doi:10.31035/cg2021045
2096-5192/© 2022 China Geology Editorial Office.

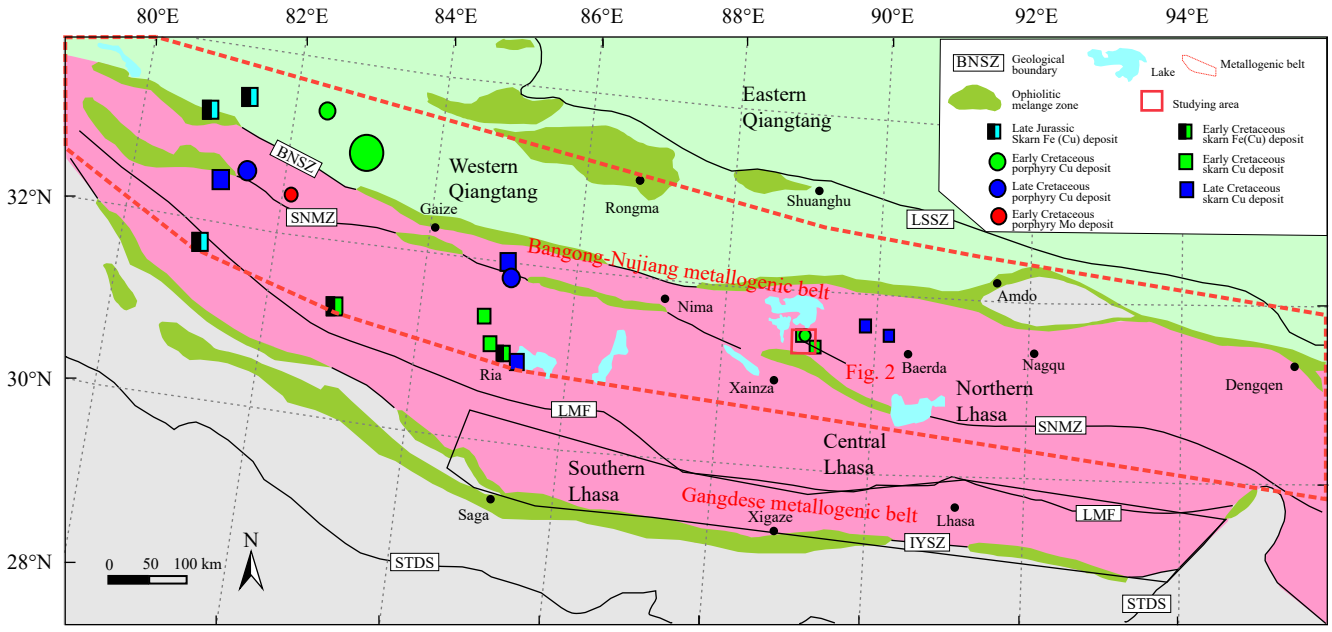

Fig. 1. Tectonic framework of the Tibetan Plateau showing the studying area (Modified from Yin A and Harrison TM, 2000; Zhu DC et al., 2016; Tang JX et al., 2021). LSSZ–Longmu Tso-Shuanghu Suture Zone; BNSZ–Bangong-Nujiang Suture Zone; SNMZ–Shiquan River-Nam Tso Mélange Zone; LMF–Luobadui-Milashan Fault; IYSZ–Indus-Yarlung Zangbo Suture Zone; STDS–South Tibetan Detachment System.

Ma tin-tungsten province in the Nanling region within an associated back-arc setting (Mao JW et al., 2021).

Geochemical anomalies are the most direct manifestation of mineralization in a region, which are used as an effective tool for deposit prospecting (Ding JS et al., 2019). Here, the authors use 1∶50000 stream sedimental geochemical exploration results for the Xiongmei area in the Northern Lhasa subterrane to reflect the mineralization anomalies arising from magmatism. These new results with the published geochemical and chronological data together, are used to constrain their geodynamics and connection with the evolution of the Northern Lhasa Terrane in BNCZ.

2. Geological background

Qinghai-Tibetan Plateau consists of the Himalaya, Lhasa, Qiangtang, and Songpan-Ganze terranes from south to north, which are separated by Indus-Yarlung Tsangpo, Bangong-Nujiang and Jinsha Suture Zones, respectively (Yin A and Harrison TM, 2000). The Lhasa Terrane (LT) and Qiangtang Terrane (QT) are located in the central Tibetan Plateau. They converged into BNCZ along the Bangong-Nujiang suture. The Bangong-Nujiang suture is characterized by a >1200 km-long east-west belt of mainly Jurassic-Cretaceous flysch, mélange, and ophiolitic fragments (Yin A and Harrison TM, 2000). Bangong-Nujiang Cu-polymetallic metallogenic belt is situated within the BNCZ, and composes a part of Tethyan metallogenic domain (Hou ZQ and Zhang HR, 2015; Li GM et al., 2017; Li XK et al., 2018b). As a famous metallogenic belt, various metal deposits were also found, such as Dulong giant porphyry Cu-Au deposit, Galale skarn Cu (Au) deposit, Jiaoxi W deposit, Shesuo skarn Cu-polymetallic deposit and Rongga Porphyry Mo deposit (Zhao YY et al., 2011; Wang Q et al., 2019b; Wang Y et al., 2019c; Peng B et al., 2019; Tang JX et al., 2021; Sun M et al., 2021; Fig. 1).

LT was further divided into the northern (NLT), central (CLT), and southern (SLT) subterranes, with the Shiquanhe-Nam Tso Mélange Zone (SNMZ) and the Luobadui-Milashan Fault (LMF) as boundaries, respectively (Fig. 1; Zhu DC et al., 2013). The study area is located in the middle segment and belonged to the NLT.

The points for the evolution of NLT can be summarized as below. One point of view is that: Before the Late Jurassic-Early Cretaceous, the Bangong-Nujiang Tethyan oceanic slab subducted to LT (Zhu DC et al., 2016); during the Late Jurassic-Early Cretaceous, Bangong-Nujiang Tethyan ocean closed through divergent subduction and resulted in the final arc-arc "soft" collision. In this stage, the cold and dense Bangong-Nujiang oceanic lithosphere below the "soft" arc-arc collision zone is rolled back (Zhu DC et al., 2016; Fan JJ et al., 2018; Li SM et al., 2018a), continued sinking resulted in the lithosphere beyond LT rupturing through gravitational instability (Wu H et al., 2015a, 2015b; Ma XD et al., 2020); During 87–76 Ma, the thickened lithospheric keel became gravitational instability and ultimately delaminated after long-term compression (Wang Q et al., 2014; Sun M et al., 2020). Another points of view are quite opposite, that the Bangong-Nujiang Tethyan oceanic slab only northward subducted (Li C et al., 2020a), and Early Cretaceous intense magmatism in the NLT resulted from the northward subducted slab break-off (Li S et al., 2019), intra-oceanic subduction (Liu DL et al., 2014), ridge-subduction (Li YL et al., 2016) or thickened lithospheric delaminated (Hu PY et al., 2017), and even Late Cretaceous intense magmatism was triggered by the far-field rollback of the northwards subducted Neo-Tethys oceanic slab (Wang ZL et al., 2021) or slab break-off (Li GM et al., 2017). And an earlier point is that Early Cretaceous intense magmatism in the NLT was the produce of the northward subduction of the Neo-Tethyan Yarlung Zangbo Ocean lithosphere (Pan GT et al.,

2006; Yin A and Harrison TM, 2000).

3. Geological features of the study area

The 1∶50000 stream sedimental geochemical exploration was carried in the Xiongmei area (Figs. 1, 2a). The strata in the study area include Early Devonian Daerdong Formation (D_1d), Early Devonian to Early Carboniferous Chaguoluoma Formation ($D_1C_1\hat{c}$), Carboniferous Yongzhu Formation ($C_{1\text{-}2}y$), Jurassic-Early Cretaceous Rila Formation (J_3K_1r), Early Cretaceous Duoni (K_1d) and Langshan Formation (K_1l). D_1d is composed of thin layer limestone and bioclastic limestone; $D_1C_1\hat{c}$ is composed of limestone; $C_{1\text{-}2}y$ is composed of quartz sandstone, shale and interbedded with limestone or calcareous sandstone; J_3K_1r is composed of thin layer limestone and bioclastic limestone; K_1d is composed of a series of volcanic-sedimentary rocks, including sandstone and argillaceous limestone interlayer, bimodal volcanics; K_1l is mainly

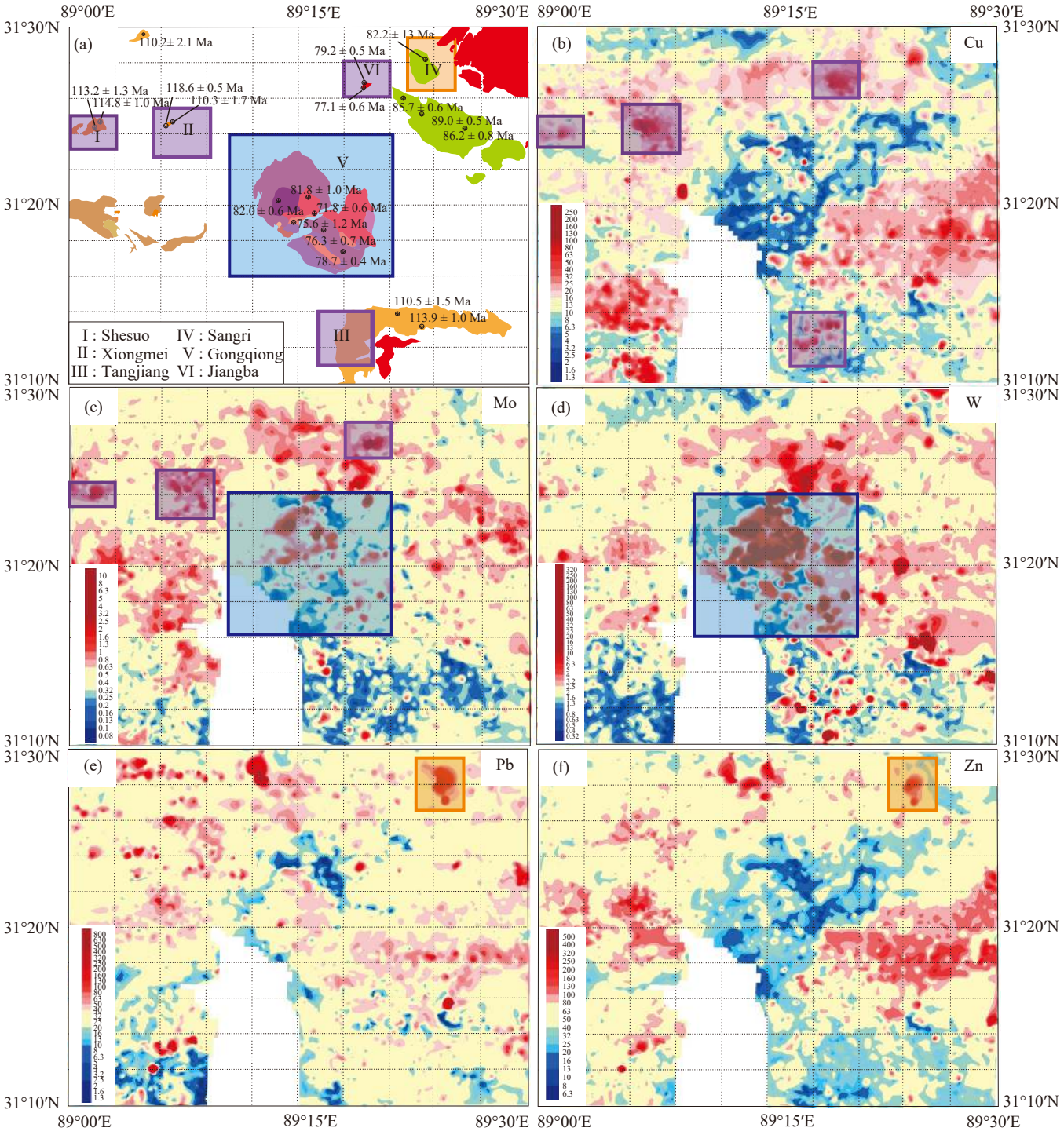

Fig. 2. Distribution map of the magmatic rocks and geochemical element anomalies in the studying area. I–Shesuo granodiorite-monzogranite plutons; II–Xiongmei granodiorite porphyries; III–Tangjiang granodiorite pluton; IV–Sangri granodiorite pluton; V–Gongqiong granodiorite-monzogranite complex massif; VI–Jiangba volcanics. The ages (Ma) of Fig. 2a are summarized in Table 1.

composed of limestone, marl limestone, and a few siltstone to silty mudstone interlayer.

Magmatic rocks mainly formed in two periods of magmatism during Early Cretaceous and Late Cretaceous respectively (Table 1; Figs. 2a, 3). Early Cretaceous magmatism was recorded by Shesuo monzogranite pluton (112–110 Ma; Yu SM et al., 2020; Sun M et al., 2021), Xiongmei granodiorite porphyry veins (110 Ma; Wang Y et al., 2019a; Yu SM et al., 2020) and Tangjiang granodiorite pluton (114 Ma; Chen W et al., 2020), while Late Cretaceous magmatism was recorded by Jiangba felsic volcanics (87–85 Ma; Sun M et al., 2020), Gongqiong granodiorite-monzogranite complex massif (82–76 Ma; Chen W et al., 2019), Sangri granodiorite pluton (79–78 Ma, Li XY et al., 2020b, or 83.2±2.3 Ma, Lin B et al., 2020).

These magmatic rocks resulted in obvious mineralization phenomena (Table 1). For example, Shesuo monzogranite intruded K_1l, and resulted in intense skarn alteration and Cu (+Mo) deposit (Sun M et al., 2021); Xiongmei granodiorite porphyry are Cu-bearing (Wang Y et al., 2019a); Tangjiang granodiorite pluton intruded into D_1d, $D_1C_1\hat{c}$, $C_{1\text{-}2}y$, and J_3K_1r, and resulted in skarnization and Cu mineralization (Chen W et al., 2020). Gongqiong granodiorite-monzogranite complex massif intruded into $D_1C_1\hat{c}$, accompanied by skarnization and greisenization, the quartz veins containing scheelite, pyrite and chalcopyrite were found in the skarn zone; the wolframite gains were found in the greisen zone (Wang Y et al., 2018).

4. Geological features of the magmatic rocks

4.1. Early Cretaceous magmatism

Zircon U-Pb dating and Hf-isotope studies indicate that the study area experienced a magmatic flare-up with strong input of mantle-derived components at ca. 114–110 Ma (Fig. 3). These magmatic rocks are characterized by high Al_2O_3 and K_2O contents, and moderate MgO content (Figs. 4a, b, c and d). The Chondrite-normalized REE patterns display right

Table 1. Age, geochemical feature and mineralization phenomena of the magmatic rocks in Xiongmei area, Tibet.

Pluton	Lithology	Age/Ma	Geochemical characteristic	Mineralization phenomena, sized	Geochemical anomaly	References
Xiongmei	Granodiorite porphyry	110–105 (Zrn); 108.4 ± 0.7 (Zrn)	SiO_2: 64.5%–68.5%; Al_2O_3: 15.0%–17.1%; MgO: 1.6%–1.9%; K_2O : 0.6%–4.7%; Sr/Y: 12.7–30.9; Y: 9.7×10^{-6}–12.7×10^{-6}; $(La/Yb)_N$: 8.0–11.8; Y_N : 5.9–8.2; enrichment in Rb, K, Th, U; depletion in Ba, Nb, Ta, Sr, Ti; $\varepsilon_{Hf}(t)$: −15.4–+3.2.	Porphyry Cu deposit; small-sized	Cu, Mo anomaly	Wang Y et al., 2019a; Yu SM et al., 2020
Shesuo	Granodiorite, monzogranite	112.1 ± 0.6 (Zrn); 110.1 ± 8.5 (Zrn); 115.2 ± 1.6 (Mo)	SiO_2: 68.9%–75.8%; Al_2O_3: 13.1%–15.4 %; MgO: 0.3%–1.4%; K_2O: 2.6%–4.9%; Sr/Y: 2.6–13.0; Y: 14.5×10^{-6}–38.1×10^{-6}; $(La/Yb)_N$: 6.1–10.5; Y_N: 8.1–21.7; enrichment in LILE; depletion in Nb, Ta and Ti; $\varepsilon_{Hf}(t)$: −15.3–+5.8	Skarn Cu-Mo deposit; small-sized	Cu, Mo anomaly	Yu SM et al., 2020; Sun M et al., 2021
Tangjiang	Granodiorite	110.5 ± 1.5 (Zrn); 110.0 ± 1.1 (Zrn), 113.9 ± 1.0 (Zrn);	SiO_2: 67.0%–64.5%; Al_2O_3: 17.0%–16.1%; MgO: 1.6%–2.1%; K_2O: 2.9%–2.5%; Sr/Y: 12.8–16.1; Y: 18.4×10^{-6}–14.3×10^{-6}; $(La/Yb)_N$: 7.8–10.1; Y_N: 8.6–11.9; enrichment in LILE; depletion in Nb, Ta and Ti; $\varepsilon_{Hf}(t)$: −3.69–+0.91.	Skarn Cu deposit; top to small sized	Cu anomaly	Chen W et al., 2020
Sangri	Granodiorite	79.2 ± 0.3 (Zrn), 77.1 ± 0.6 (Zrn); 83.2 ± 2.3 (Grt)	SiO_2: 65.2%–69.6%; Al_2O_3: 15.0 %–15.9%; MgO: 1.0%–1.6%; K_2O: 2.1%–3.7%; Sr/Y: 29.8–41.0; Y: 22.0×10^{-6}–35.7×10^{-6}; $(La/Yb)_N$: 10.2–23.4; Y_N: 6.5–8.3; enrichment in LILE; depletion in Nb, Ta and Ti.	Skarn Cu deposit; unknown	Cu, Mo anomaly	Li XY et al., 2020; Lin B et al., 2020
Gongqiong	Granodiorite, monzogranite	71.8±0.6 (Zrn), 75.6±1.2 (Zrn)	SiO_2: 67.8%–73.1%; Al_2O_3: 13.1%–15.1%; MgO: 0.5%–2.0%; K_2O: 3.8%–5.1%; Sr/Y: 5.3–8.1; Y: 12.0×10^{-6}–14.4×10^{-6}; $(La/Yb)_N$: 14.0–32.7; Y_N: 12.2–20.8; enrichment in Rb, K, Th, U; depletion in Ba, Nb, Ta, Sr, Ti; $\varepsilon_{Hf}(t)$: −0.5–+2.5.	Scheelite-bearing quartz veins; wolframite in the greisen; mineralization point	W anomaly	Wang Y et al., 2018; Chen W et al., 2019
Jiangba	Andesite, dacite,	87.1 ± 1.1 (Zrn), 85.1 ±1.0 (Zrn),	SiO_2: 61.4%–70.8%; Al_2O_3: 13.4%–17.4%; MgO: 1.4%–2.8%; K_2O: 1.9%–3.0%; Sr/Y: 30.0–63.6; Y: 8.7×10^{-6}–19.3×10^{-6}; $(La/Yb)_N$: 17.9–24.3; Y_N : 4.6–9.3; enrichment in LILE; depletion in Nb, Ta and Ti; $\varepsilon_{Hf}(t)$: +2.7 – +7.1.	No found	Pb, Zn anomaly	Sun M et al., 2020
Jiangba	Rhyolite	81.6 ± 0.5 (Zrn)	SiO_2: 74.6%–76.4%; Al_2O_3: 12.0%–13.6%; MgO: 0.2%–0.5%; K_2O: 3.2%–7.2%; Sr/Y: 30.0–63.6; Y: 0.7×10^{-6}–3.0×10^{-6}; $(La/Yb)_N$: 3.8–5.6; Y_N: 22.5–25.3; enrichment in LILE; depletion in Nb, Ta and Ti; $\varepsilon_{Hf}(t)$: +1.0–+3.5.	No found		Sun M et al., 2020

Notes: Zrn means zircon U-Pb dating; Mo means molybdenite Re-Os isochron age; Grt means garnet U-Pb dating.

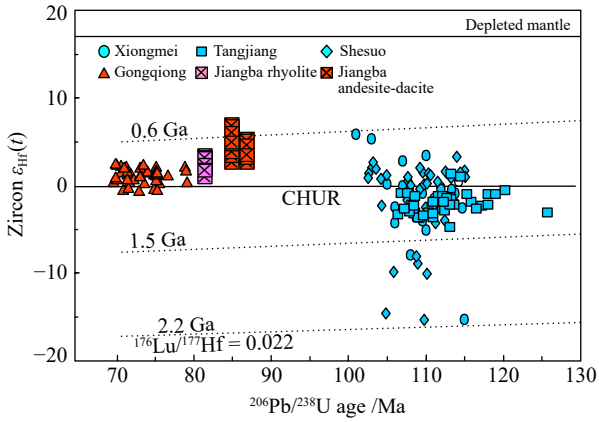

Fig. 3. Zircon $^{206}Pb/^{207}Pb$ age *vs.* $\varepsilon_{Hf}(t)$ values diagram for the magmatic rocks.

sloping patterns and fractionated REE, On the primitive-mantle-normalized spider diagram (Fig. 5a), the rocks are commonly characterized by the relative depletion in Nb, Ta, Ba, Sr, and Ti and the significant enrichment in LILEs, such as Th, U, K, and Pb (Fig. 5b).

These Early Cretaceous magmatic rocks display varied εHf(t) values (Table 1; Xiongmei: −15.4–+3.2; Shesuo: −15.3–+5.8; Tangjiang: −3.69–+0.91).

4.2. Late Cretaceous magmatism

Zircon U-Pb dating indicates a intense magmatism occurred during 87–76 Ma, which lasted 11 m.y., and the Hf-isotope from these magmatic rocks implies that strong input of mantle-derived components and juvenile crust remelt (Fig. 3). They have similar geochemical features as Early Cretaceous magmatism, with high Al_2O_3 and K_2O contents, moderate MgO content (Figs. 4a, b, c and d), fractionated REE patterns and depletion in HFSEs as well as enrichment in LILEs (Figs. 5c, d).

These Late Cretaceous magmatic rocks display varied $\varepsilon_{Hf}(t)$ values (Table 1; Gongqiong: −0.5–+2.5; Jiangba andesite-dacite: +2.7–+7.1; Jiangba rhyolite: +1.0–+3.5)

5. Geochemical anomalies associate with magmatism

Determining threshold is one of fundamental tasks for analyzing the geochemical data of stream sediments, then delineate geochemical anomalies, analyze and identify the

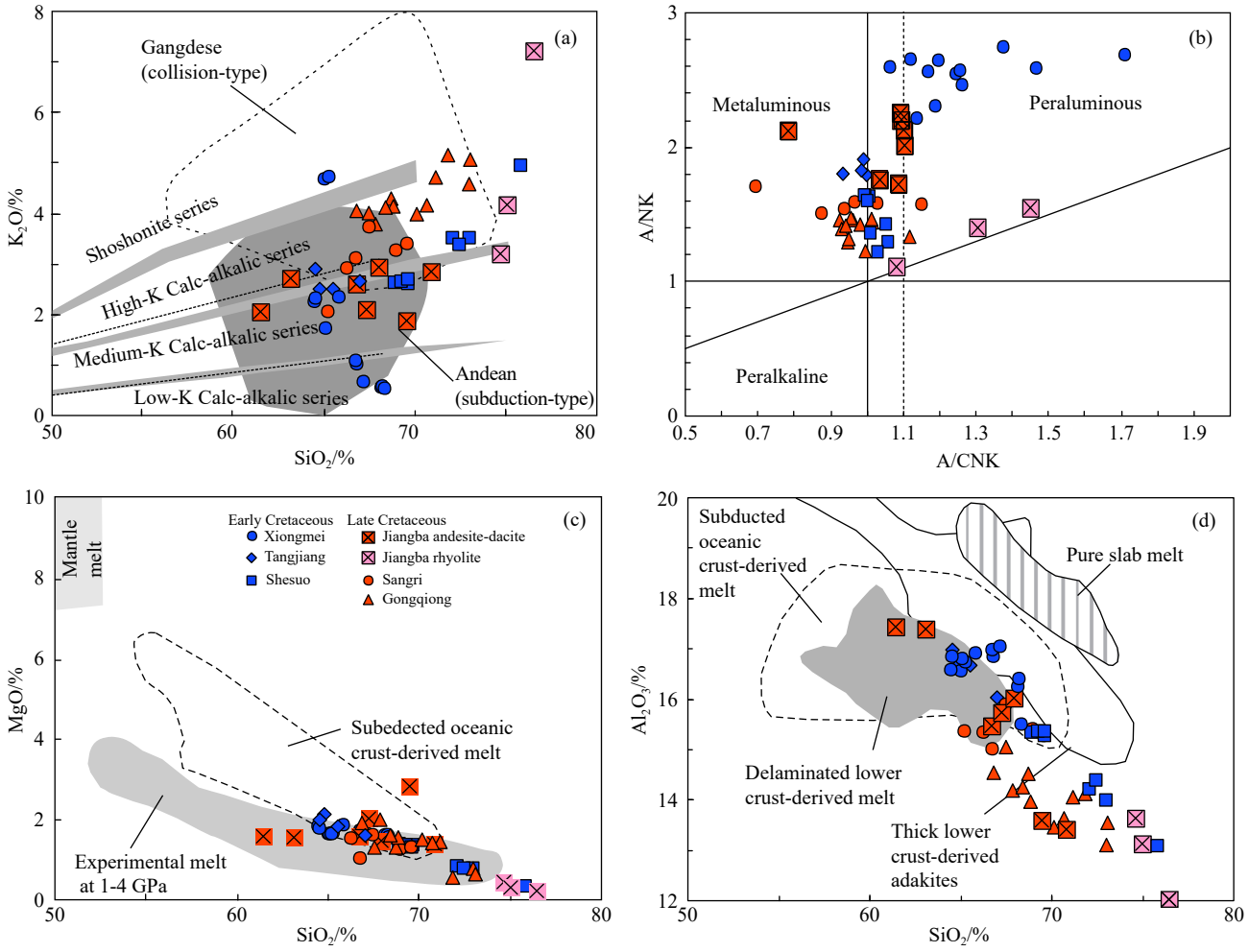

Fig. 4. Some discrimination diagrams for the magmatic rocks. a–K_2O-SiO_2 diagram (modified from Zhu XS et al., 2017); b– A/NK *vs.* A/CNK diagram; c–MgO and SiO_2 diagram (modified from Rapp PR and Watson EB, 1995); d –Al_2O_3 and SiO_2 diagram. The legend was same as the Fig. 3.

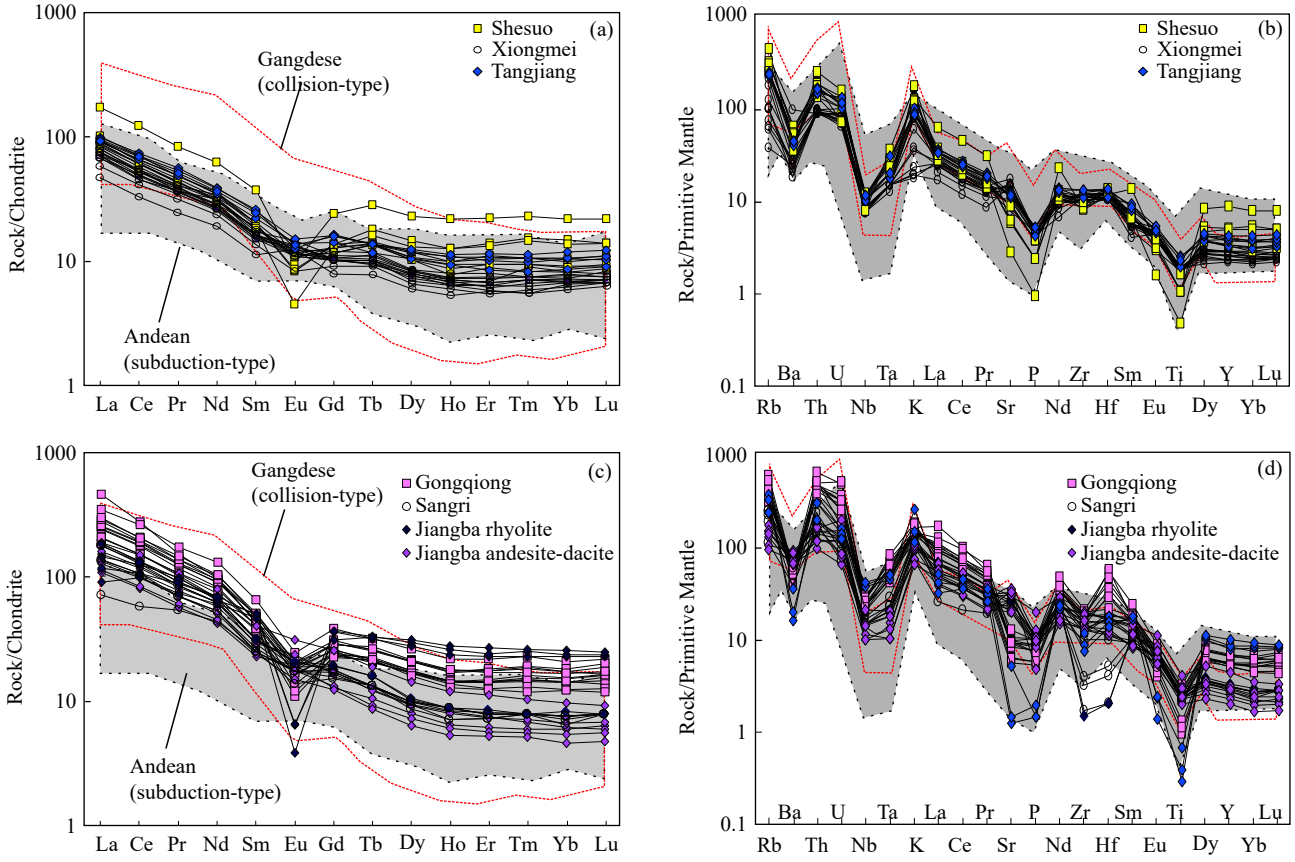

Fig. 5. Chondrite-normalized REE diagrams and primitive mantle (PM) normalized trace element diagrams. The scope for the Gangdese and Andean are modified from Zhu XS et al., 2017.

mineralization anomalies, so as to provide an effective basis for further prospecting. Geochemical anomalies for the metallogenic elements of Cu, Mo, W, Pb and Zn were circumscribed in geochemical exploration area. The sampling area is about 1600 km^2, and 6586 valid samples were obtained, the sampling density is 4.1 piece/km^2. Detailed sampling and data processing procedures have been described in Ding JS et al. (2019) and it was reworded in Appendix 1.

In this paper, the average content and standard deviation of five ore-forming elements in Xiongmei area are obtained by iterative elimination of outlier-data-points and statistical analysis. The theoretical anomaly lower limit is obtained according to the sum of the average content and 1.65 times the standard deviation, and then the actual anomaly lower limit is determined in combination with the actual geology and mineral resources in the area. The abnormal outer, middle and inner band of each element are respectively delineated by 1, 2 and 4 times of the lower limit, and the abnormal map of each element is made using the DTM analysis module of the MapGIS platform (Fig. 2). After calculation, single element anomaly lower limit are as below: Cu ($\times10^{-6}$): 30; Mo ($\times10^{-6}$): 1; W ($\times10^{-6}$): 4; Pb ($\times10^{-6}$): 60; Zn ($\times10^{-6}$): 120.

As shown in Fig. 2, the circled geochemical anomalies are almost around the pluton and volcanics. Considering that there is less rainfall in the studying area, the factors causing geochemical anomalies are basically in situ. The highly coupling between the geochemical anomalies and the pluton and volcanics suggest that these anomalies resulted from the related magmatisms. The coupling relations are regular as below (Table 2): Cu element geochemical anomalies are spatial coincidence with Early Cretaceous Shesuo granodiorite-monzogranite plutons (Peak value: 99×10^{-6}; Average value: 31×10^{-6}), Xiongmei granodiorite porphyries plutons (Peak value: 216×10^{-6}; Average value: 56×10^{-6}), Tangjiang granodiorites plutons (Peak value: 98×10^{-6}; Average value: 29×10^{-6}) and Late Cretaceous Sangri granodiorite plutons (Peak value: 154×10^{-6}; Average value: 45×10^{-6}) (Fig. 2b); Mo element geochemical anomalies are spatial coincidence with Shesuo granodiorite-monzogranite (Peak value: 3.5×10^{-6}; Average value: 0.6×10^{-6}), Xiongmei granodiorite porphyries (Peak value: 3.3×10^{-6}; Average value: 1.0×10^{-6}), Late Cretaceous Sangri granodiorite plutons (Peak value: 13×10^{-6}; Average value: 1.5×10^{-6}), part of the Gongqiong granodiorite-monzogranite complex massif (Peak value: 12×10^{-6}; Average value: 1.7×10^{-6}) (Fig. 2c); Tungsten element geochemical anomalies are spatial coincidence with Late Cretaceous Gongqiong granodiorite-monzogranite complex massif (Peak value: 751×10^{-6}; Average value: 69×10^{-6}) (Fig. 2d); Pb and Zn element geochemical anomalies are spatial coincidence with the Late Cretaceous Jiangba dacite-andesite volcanics and one unknown volcanics (Peak value: Pb: 619×10^{-6}, Zn: 427×10^{-6}; Average value: Pb: 167×10^{-6}, Zn: 137×10^{-6}) (Figs. 2e, f).

Table 2. Peak and average value of the geochemical anomalies arising from pluton and volcanics.

Pluton	Peak/10^{-6}	Average /10^{-6}	Background (lower value)/10^{-6}	Intensity of anomaly (Peak/ Background)
Abnormal element: Cu				
Shesuo	99	31	30	3.3
Xiongmei	216	56	30	7.2
Tangjiang	98	29	30	3.2
Sangri	154	45	30	5.1
Abnormal element: Mo				
Shesuo	3.5	0.6	1	3.5
Xiongmei	3.3	1.0	1	3.3
Sangri	13	1.5	1	13
Gongqiong	12	1.7	1	12
Abnormal element: W				
Gongqiong	751	69	4	187.8
Abnormal element: Pb				
Jiangba	619	167	60	10.3
Abnormal element: Zn				
Jiangba	427	137	120	3.5

6. Discussion

6.1. Constrains on the evolution of BNCZ

Xiongmei area is located to the northern side of the Shiquanhe-Nam Tso Mélange Zone (Fig. 1). If Early Cretaceous magmatism in the NLT was the produce of the northward subduction of the Yarlung Zangbo Ocean lithosphere, and Shiquanhe-Nam Tso Mélange Zone represents back-arc basin (Pan GT et al., 2006; Yin A and Harrison TM, 2000), the mineralization in Xiongmei area should be tin-tungsten belt (Mao JW et al., 2021). Actually, Early Cretaceous magma mainly resulted in Cu, Mo mineralization the studying area (Figs. 2a–c).

Cu mineralization are associated with Cretaceous granodiorite or granodiorite porphyry, monzogranite in Xiongmei area, these Cu mineralization are like porphyry-skarn Cu deposits (Wang Y et al., 2019a; Lin B et al., 2020; Sun M et al., 2021). Typical porphyry-skarn Cu deposits (PCD) are always found in island- and continental-arc, post-collisional setting and sometimes intracontinental environment (Richards JP, 2003, 2009; Sillitoe RH, 2010; Yuan SD et al., 2018; Yazdi Z et al., 2019). Compared the PCDs in Gangdise metallogenic belt (typical collision-type) with the Andean metallogenic belt (typical subduction-type), the collision-type have higher Sr/Y and $(La/Yb)_N$ values, K_2O, SiO_2, and relative lower Y and Yb contents, than the subduction-type (Figs. 4a, 5a, c, 6; Zhu XS et al., 2017), since the collision-type PCDs result from remelting of sulfide-bearing cumulates inherited from arc magma by asthenosphere upwelling and post-collisional thickening (Richards JP, 2014; Hou ZQ et al., 2015; Wan B et al., 2018). Some geochemical features of Early Cretaceous Xiongmei, Shesuo and Tangjiang pluton and Late Cretaceous Sangri pluton are according with subduction-type (Figs. 4a, 5), but moderated MgO contents (Fig. 4c) and enriched Hf isotope composition (Fig. 3) of them are completely different from the melt from slab or metasomatic mantle wedge during subduction.

Due to the residue of plagioclase, Sr and Eu concentrations tend to be significantly low in melts generated at low pressures, while due to the residue of garnet, while HREEs and Y tend to be significantly lower in melts generated at high pressures (Moyen JF, 2009). The relatively low Sr/Y and $(La/Yb)_N$ value imply that these Cu mineralization magma generated from decompression melting in an extensional environment (Wang Y et al., 2019a; Yu SM et al., 2020), which is not consistent with a typical post-collision PCD formed in collisional thicken crust. Slab break-off thicken crust delamination are common extensional environments that can formed PCDs (Richards JP, 2009, 2011; Shafiei B et al., 2009; Hou ZQ et al., 2015). If two phase of delamination or slab break-off happened during short time in the same location, it is fundamentally unfeasible, and the post-collisional slab break-off always happened before thicken crust delamination in intracontinental environment.

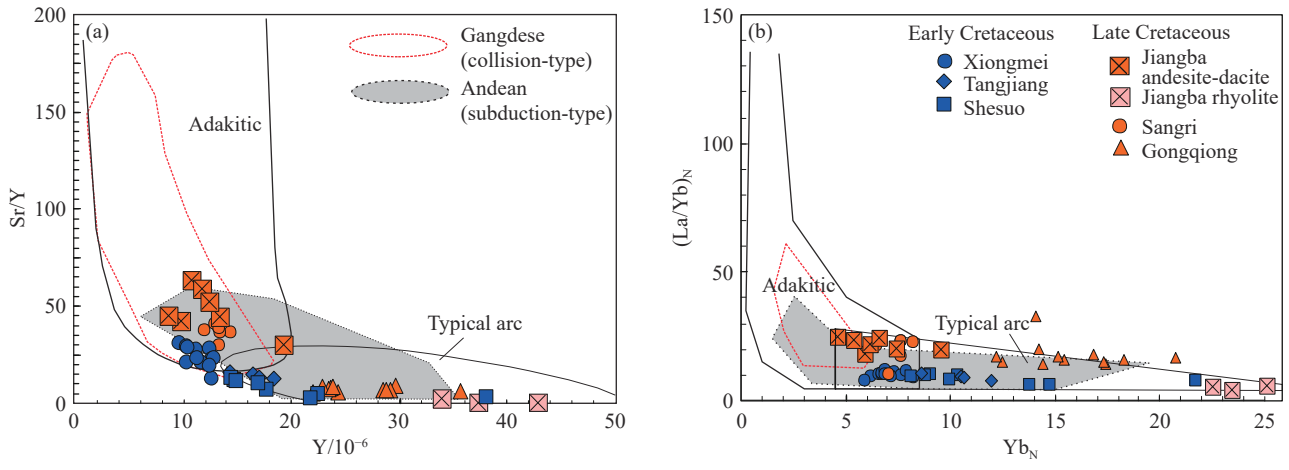

Fig. 6. a–Sr/Y *vs.* Y and b–$(La/Yb)_N$ *vs.* Yb_N diagrams. The scope for the Gangdese and Andean are modified from Zhu XS et al., 2017 and Wan B et al., 2018.

Thus the best explanation is that Early Cretaceous phase was associated with slab break-off while Late Cretaceous phase was associated with delamination.

As tungsten is a kind of high-temperature element, the tungsten mineralization is always associated with high-temperature hydrothermal that generated from differentiated complex massif. The Gongqiong complex massif experienced a highly differentiated evolution from 82.0–75.7 Ma (Fig. 3d; Chen W et al., 2019), which needed an extensional environment (Li XF et al., 2008; Hou ZQ and Zhang HR, 2015). The Hf isotopic compositions and geochemistry of Gongqiong complex massif implies that the magma sourced from a mafic lower crust (Chen W et al., 2019). A prolonged, high-temperature extensional environment is essential for the Late Cretaceous tungsten mineralization. Both batch delamination and post-collision extension model are suitable for this requirement.

Pb-Zn deposits are always sourced from the ancient crust or host strata (Marchev P et al., 2005; Sun JD et al., 2018). Though the Pb-Zn geochemical anomalies have been identified around Late Cretaceous Jiangba volcanics (Fig. 2f, g), Pb-Zn mineralization has not been found. We assume that this anomaly was sourced from the wallrock strata when the Jiangba volcanics emplacement, it implies the lead and Zinc contents in magma for Jiangba volcanics are low, and the ancient crust mixing is limited. Jiangba volcanics can be divided into andesite-dacite and rhyolite series. The andesite-dacites have adakitic signatures and high MgO contents, while rhyolites have non-adakitic signatures and low MgO contents, both of them have high positive $\varepsilon Hf_{(t)}$ values (andesite-dacites: +2.7–+7.1; rhyolites: +1.0–+3.5). Combined, andesite-dacite series are sourced from a juvenile mafic lower crust foundered into the convecting mantle, melted, and interacted with peridotite, while the rhyolites were derived by a juvenile mafic lower crust. Post-collision thickened juvenile crust delamination is first considered for the Jiangba volcanics forming (Sun M et al., 2020).

6.2. A model for the evolution of Northern Lhasa terrane

Three episodes of magmatism occurred in the NLT, namely, the Jurassic (170–150 Ma), Early Cretaceous (125–100 Ma), and Late Cretaceous (90–68 Ma). Early Cretaceous magmatism consists of a near East-West trending A2-type granite belt (Ma XD et al., 2020), bimodal volcanics (Sui QL et al. 2013; Chen Y et al., 2014), norite plutons (Ma XD et al., 2020), several high-Mg andesites/diorite and adakitic rocks (Wu H et al., 2015a, 2015b; Wang W et al., 2020) and abundant alkali-rich I-type granite (Chen Y et al., 2014). These rocks suggest that a high temperature extensional setting associated with asthenosphere upwelling existed along the northern margin of the Lhasa terrane (Luo AB et al., 2021). A series of special types were identified from the Late Cretaceous magmatism, consisting of bimodal volcanic rocks, mafic dikes, high-Mg# adakitic rocks, Mg-rich andesite-dacite and Cu-bearing porphyrites (Wang Q et al., 2014; Lei M et al., 2020). These rocks suggest that a compressional to an intracranial extensional environmental change accompanying asthenosphere upwelling happened.

After discussion on the geochemical exploration and petrogeochemical characteristics of magmatic rocks in Xiongmei area, we can draw the inferences as below: A Cu-rich juvenile crust has been formed at the bottom of NLT before ca. 125 Ma, which is the source for Early and Late Early Cu mineralization; During 120–105 Ma and 89–76 Ma, the asthenosphere mantle was upwelling, the NLT was in an extensional and high-temperature environment.

Based on these inferences, we sketch out a reasonable model for the evolution of the Northern Lhasa terrane, and show it in Fig. 7.

Before ca. 125 Ma, Bangong-Nujiang oceanic slab southwards subducted beyond the Lhasa terrane. Abundant arc magma formed, and melt and fluid from the subducted slab continuing metasomatized the overlying mantle wedge. At sometime nearly 125 Ma, the slab began rolling back, asthenosphere slowly upwelling due to volume compensating, the subduction-modified lithospheric mantle wedge melted to the Cu-rich juvenile crust (Fig. 7a).

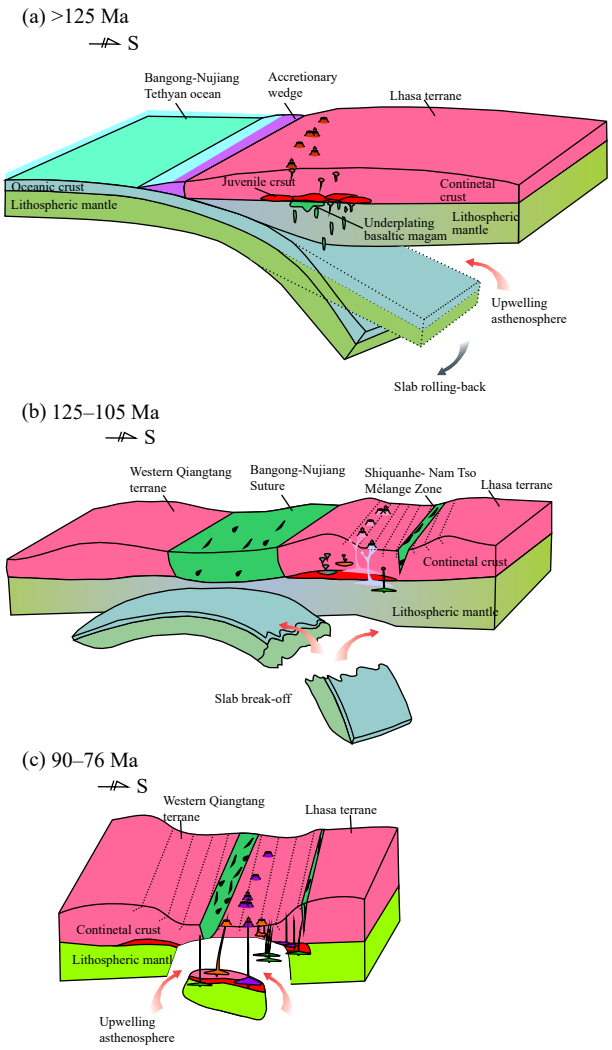

Fig. 7. Schematic illustration shows the geodynamic evolution of the NLT.

During 120–105 Ma, at the end of the slab rolling back, the slab break-off happened. Under the slab break-off setting, the asthenosphere upwelled through the slab window, causing large-scale overlying lithosphere melting (Fig. 7b). Cu-rich juvenile and ancient crust were melt and mixed into the Xiongmei, Shesuo and Tangjiangqiongguo plutons. These pluton are associated with Cu and Mo mineralization (Figs. 2a–c).

There is almost no ca. 105–90 Ma magmatic activity. This 10 Myr magmatic hiatus reflects the collision between Lhasa and Qiangtang terranes continuing.

During 90–76 Ma, after nearly 10 Myr collisional thicken continuing, the lithosphere beneath the NLT became gravitational instability and happened delaminated (Fig. 7c). The delaminated lithosphere sinked into the asthenosphere and melted. These melt are characterized by the high Sr/Y vales and MgO content like Jiangba andesite-dacite; meanwhile asthenosphere upwelled following the channel left by the delaminated lithosphere, the overlying lithosphere was heated and melted to form Jiangba rhyolites and Gongqiong pluton. The Pb-Zn anomalies are resulted from the Jiangba felsic volcanics emplacement, the W mineralizations are associated with the Gongqiong pluton. The residual Cu-rich juvenile melted to form Sangri pluton and resulted in the Cu, Mo mineralizations.

7. Conclusion

In the study area, Early Cretaceous magma mainly resulted in Cu, Mo mineralization, Late Cretaceous magma mainly resulted in Cu, Mo, and W mineralization. According to the feature of mineralization and magmatism, a evolution model is proposed for the northern Lhasa terrane, involving a southward subduction, slab rolling back and break-off and thicken crust delamination from Jurassic to Late Cretaceous.

CRediT authorship contribution statement

Xu-dong Ma conceived of the presented idea. Shi-mian Yu, Yan-chun Hu, Wei Chen, Qing-ping Liu, Yang Song, Ju-xing Tang wrote the manuscript in consultation. All authors discussed the results and contributed to the final manuscript.

Declaration of competing interest

The authors declare no conflicts of interest.

Acknowledgment

Financial support was provided by the program of China Geological Survey (DD20190167) and National Natural Science Foundation of China (41902099). The authors would like to thank the reviewers and editors very much for their constructive comments.

Supplementary materials

Sampling, analytical methods, and mapping

Sampling

According to the specifications and technical requirements of 1∶50000 geochemical survey, the authors carried out 1∶50000-scale stream sediments survey in the study area. The authors collected 6585 effective samples in the range of 160 km^2, equivalent to an average sampling density of 4 spot/km^2. These samples were mainly fine to medium sand with a particle size of 60 mesh. The sampling points were mainly distributed in the first and second order water systems or gullies, and soil samples were used in some areas where the gullies were not developed. After drying and sieving, the sample was collected by "point-centred quarter method" in paper bags with the weight of each sample no less than 200 g.

Analytical methods

The analysis and test of the geochemical datasets in this study was undertaken by the Guangdong Province Research Center for Geoanalysis. The analysis of these samples adopted an advanced analysis system and supporting scheme: Concentrations of Cu, Pb and Zn were determined by inductively coupled plasma optical emission spectrometry; Concentrations of W and Mo were determined by inductively coupled plasma mass spectrometry. In the above analysis methods, the detection limit of each element met or was better than the detection limit requirements of the Chinese Geochemical Survey Specifications of DZ/T 0130-2006 and DZ/T 0011-2015. The following were the detection limits for 6 elements: Cu (1 μg/g), Mo (0.02 μg/g), Pb (1 μg/g), Zn (2 μg/g), W (0.02 μg/g).

The qualities control of the samples were based on the Chinese Geochemical Survey Specifications of DZ/T 0130-2006 and DZ/T 0011-2015 (Table 3). Geochemical sample percent of report of each element was more than 94.7%. Logarithmic differences (ΔlogC) and Relative standard deviation (RSD) between the analytical values and the recommended values of the National First-level Certified Reference Stream Sediments (GBW) were calculated to measure the bias:

$$\Delta \lg \overline{C}(\mathrm{GBW}) = \left| \lg \overline{C_i} - \lg C_S \right|$$

$$\mathrm{RSD(GBW)} = \frac{\sqrt{\dfrac{\sum_{i=1}^{n} (C_i - C_s)^2}{n-1}}}{C_s} \times 100\%$$

Where $\bar{C}_i$ is the measured average value of each standard sample (GBW); C_i is the single determined value of the GBW; C_s is the recommended value of the GBW; and n is the measurement times of each standard sample. Table 1 lists the values of Δlog $\bar{C}$(GBW) and RSD (GBW) of geochemical data for different concentration ranges.

The accuracy and precision of various methods were verified by standard materials, and the results were in line with Chinese Geochemical Survey Specifications of DZ/T 0130-2006 and DZ/T 0011-2015.

Mapping

According to the Chinese Geochemical Survey Specifications of DZ/T 0167-2006, in order to traced the

Table 3. Allowance of bias of the analysis of first standard samples (c.f., Chinese Geochemical Survey Specifications of DZ/T 0130-2006 and DZ/T 0011-2015).

Concentration range	Δlog C̄(GBW)	RSD(GBW)
<3 Detection limit	≤0.13	≤15%
>3 Detection limit	≤0.11	≤10%
≥1%	≤0.07	≤7%

extension of geochemical baselines on the geochemical map and understood the geological significance, we used the cumulative frequency method and adjusted the color levels to make the geochemical map of each element (Fig. 2).

References

Chen W, Song Y, Liu HZ, Sun M, Ma XD, Ding JS, Li XY. 2019. MMEs formed by magma mixing of different episodes of the same sourced magma: A case study of the Late Cretaceous Sangxinri pluton in the middle part of the northern Lhasa Block. Acta Petrologica Sinica, 35(7), 2143–2157 (in Chinese with English abstract). doi: 10.18654/1000-0569/2019.07.12.

Chen W, Song Y, Qu XM, Sun M, Ding JS, Ma XD. 2020. MMEs in the Tangjiangqiongguo pluton in the North Lhasa Block formed by magma mixing of different episodes of the same sourced magma: A new petrogenetic model for the MMEs. Earth Science, 45(1), 17–30 (in Chinese with English abstract). doi: 10.3799/dqkx.2018.263.

Chen Y, Zhu DC, Zhao ZD, Meng FY, Wang Q, Santosh M, Wang LQ, Dong GC, Mo XX. 2014. Slab breakoff triggered ca. 113 Ma magmatism around Xainza area of the Lhasa Terrane, Tibet. Gondwana Research, 26(2), 449–463. doi: 10.1016/j.gr.2013.06.005.

Ding JS, Chen W, Zhou H, Guo QQ, Sun M, Zhang Y. 2019. Geochemical characteristics from 1:50000 survey data of stream sediments and ore –search prospects in the Xiongmei area, Tibet. Geology and Exploration, 55(1), 48–63 (in Chinese with English abstract). doi: 10.12134/j.dzykt.2019.01.005.

Fan JJ, Li C, Sun ZM, Xu W, Wang M, Xie CM. 2018. Early Cretaceous MORB-type basalt and A-type rhyolite in northern Tibet: Evidence for ridge subduction in the Bangong–Nujiang Tethyan ocean. Journal of Asian Earth Sciences, 154, 187–201. doi: 10.1016/j.jseaes.2017.12.020.

Hou ZQ, Zhang HR. 2015. Geodynamics and metallogeny of the eastern Tethyan metallogenic domain. Ore Geology Reviews, 70, 346–384. doi: 10.1016/j.oregeorev.2014.10.026.

Hou ZQ, Yang ZM, Lu YJ, Kemp A, Zheng YC, Li QY, Tang JX, Yang ZS, Duan LF. 2015. A genetic linkage between subduction and collision-related porphyry Cu deposits in continental collision zones. Geology, 43(3), 247–250. doi: 10.1130/G36362.1.

Hu PY, Zhai QG, Jahn BM, Wang J, Li C, Chung SL, Lee HY, Tang SH. 2017. Late Early Cretaceous magmatic rocks (118-113 Ma) in the middle segment of the Bangong-Nujiang suture zone, Tibetan Plateau: Evidence of lithospheric delamination. Gondwana Research, 44, 116–138. doi: 10.1016/j.gr.2016.12.005.

James DE, Sacks IS. 1999. Cenozoic formation of the Central Andes: A geophysical perspective, in Skinner B (ed), Geology and Ore Deposits of the Central Andes: Society of Economic Geologists Special Publication 7, l–25.

Kapp P, DeCelles PG. 2019. Mesozoic-Cenozoic geological evolution of the Himalayan-Tibetan orogen and working tectonic hypotheses. American Journal of Science, 319(3), 159–254. doi: 10.2475/03.2019.01.

Kay SM, Mpodozis C, Coira B. 1999. Magmatism, tectonism, and mineral deposits of the Central Andes (22°–33°S), in Skinner B (ed), Geology and Ore Deposits of the Central Andes: Society of Economic Geologists Special Publication 7, 27–59.

Lehmann B. 2004. Metallogeny of the Central Andes: Geotectonic framework and geochemical evolution of porphyry systems in Bolivia and Chile during the last 40 million years. Metallogeny of the Pacific Northwest: Tectonics, Magmatism and Metallogeny of Active Continental Margins, 118–122.

Lei M, Chen JL, Xu JF, Zeng YC, Xiong QW. 2020. Late Cretaceous magmatism in the NW Lhasa Terrane, southern Tibet: Implications for crustal thickening and initial surface uplift. GSA Bulletin, 132(1–2), 334–352. doi: 10.1130/B31915.1.

Li C, Wang GH, Zhao ZB, Du JX, Ma XX, Zheng YL. 2020. Late Mesozoic tectonic evolution of the central Bangong-Nujiang Suture Zone, central Tibetan Plateau. International Geology Review, 62(18), 2300–2323. doi: 10.1080/00206814.2019.1697859.

Li XY, Qu XM, Ma XD, Chen W, Sun M. 2020. Chronology, types and genesis of post-collisional copper bearing magmatic rocks in the Xiongmei area, the middle part of Bangong Co-Nujiang metallogenic belt. Acta Geological Sinica, 94(4), 1264–1281 (in Chinese with English abstract).

Li S, Yin C, Guilmette C, Ding L, Zhang J. 2019. Birth and demise of the Bangong-Nujiang Tethyan Ocean: A review from the Gerze area of central Tibet. Earth-Science Reviews, 198, 102907. doi: 10.1016/j.earscirev.2019.102907.

Li SM, Wang Q, Zhu DC, Stern RJ, Cawood PA, Sui QL, Zhao Z. 2018. One or two Early Cretaceous arc systems in the Lhasa Terrane, southern Tibet. Journal of Geophysical Research: Solid Earth, 123(5), 3391–3413. doi: 10.1002/2018JB015582.

Li XK, Chen J, Wang RC, Li C. 2018. Temporal and spatial variations of Late Mesozoic granitoids in the SW Qiangtang, Tibet: Implications for crustal architecture, Meso-Tethyan evolution and regional mineralization. Earth-Science Reviews, 185, 374–396. doi: 10.1016/j.earscirev.2018.04.005.

Li GM, Qin KZ, Li JX, Evans NJ, Zhao JX, Cao MJ, Zhang XN. 2017. Cretaceous magmatism and metallogeny in the Bangong-Nujiang metallogenic belt, central Tibet: Evidence from petrogeochemistry, zircon U-Pb ages, and Hf-O isotopic compositions. Gondwana Research, 41, 110–127. doi: 10.1016/j.gr.2015.09.006.

Li YL, He J, Han ZP, Wang CS, Ma PF, Zhou A, Liu SA, Xu M. 2016. Late Jurassic sodium-rich adakitic intrusive rocks in the southern Qiangtang terrane, central Tibet, and their implications for the Bangong –Nujiang Ocean subduction. Lithos, 245, 34–46. doi: 10.1016/j.lithos.2015.10.014.

Li XF, Yasushi W, Hua RM, Mao JW. 2008. Mesozoic Cu-Mo-W-Sn mineralization and ridge/triple subduction in South China. Acta Geologica Sinica, 82(5), 625–640 (in Chinese with English abstract).

Lin B, Chen L, Liu ZY, Tang JX, Zou B, He W. 2020. Constrains on the geochronology of porphyry-skarn copper deposit from U-Pb dating of garnet: A case study of the Sangri copper deposit, Tibet. Acta Geological Sinica, 94(10), 2883–2892 (in Chinese with English abstract). doi: 10.19762/j.cnki.dizhixuebao.2020030.

Liu DL, Huang QS, Fan SQ, Zhang LY, Shi RD, Ding L. 2014. Subduction of the Bangong –Nujiang Ocean: Constraints from granites in the Bangong Co area, Tibet. Geological Journal, 49(2), 188–206. doi: 10.1002/gj.2510.

Liu YM, Wang M, Li C, Xie CM, Chen HQ, Li YB, Fan JJ, Li XK, Xu W, Sun ZM. 2017. Cretaceous structures in the Duolong region of central Tibet: Evidence for an accretionary wedge and closure of the Bangong –Nujiang Neo-Tethys Ocean. Gondwana Research, 48, 110–123. doi: 10.1016/j.gr.2017.04.026.

Luo AB, Wang M, Zeng XW, Hao YJ, Li H. 2021. An extensional collapse model for the Lhasa-Qiangtang orogen in Central Tibet. Gondwana Research, 89, 66–87. doi: 10.1016/j.gr.2020.08.016.

Ma XD, Song Y, Tang JX, Chen W. 2020. Newly identified rhyolite-biotite monzogranite (A2-type granite)-norite belt from the Bangong-Nujiang collision zone in Tibet Plateau: Evidence for the slab break-

off beneath the Lhasa Terrane. Lithos, 366, 105565. doi: 10.1016/j.lithos.2020.105565.

Mao JW, Zheng W, Xie GQ, Lehmann B, Goldfarb R. 2021. Recognition of a Middle-Late Jurassic arc-related porphyry copper belt along the southeast China coast: Geological characteristics and metallogenic implications. Geology, 49(5), 592–596. doi: 10.1130/G48615.1.

Marchev P, Kaiser-Rohrmeier M, Heinrich C, Ovtcharova M, von Quadt A, Raicheva R. 2005. 2: Hydrothermal ore deposits related to post-orogenic extensional magmatism and core complex formation: The Rhodope Massif of Bulgaria and Greece. Ore Geology Reviews, 27(1–4), 53–89. doi: 10.1016/j.oregeorev.2005.07.027.

Moyen JF. 2009. High Sr/Y and La/Yb ratios: The meaning of the "adakitic signature". Lithos, 112(3–4), 556–574. doi: 10.1016/j.lithos.2009.04.001.

Pan GT, Mo XX, Hou ZQ, Zhu DC, Wang LQ, Li GM, Zhao ZD, Geng QR, Liao ZL. 2006. Spatial–temporal framework of the Gangdese Orogenic Belt and its evolution. Acta Petrologica Sinica, 22(3), 521–533 (in Chinese with English abstract). doi: 10.3969/j.issn.1000-0569.2006.03.001.

Peng B, Li BL, Liu HY, Qin GZ, Gong FZ, Zhou L. 2019. Main collisional mineralization of Bangong-Nujiang metallogenic belt, Tibet: Geochronological, geochemical and isotopic evidence from Rongga molybdenum deposit. Acta Petrological Sinica, 35(3), 705–723 (in Chinese with English abstract). doi: 10.18654/1000-0569/2019.03.06.

Rapp RP, Watson EB. 1995. Dehydration melting of metabasalt at 8–32 kbar: Implications for continental growth and crust-mantle recycling. Journal of Petrology, 36(4), 891–931. doi: 10.1093/petrology/36.4.891.

Richards JP. 2003. Tectono-magmatic precursors for porphyry Cu-(Mo-Au) deposit formation. Economic Geology, 98(8), 1515–1533. doi: 10.2113/gsecongeo.98.8.1515.

Richards JP. 2009. Postsubduction porphyry Cu-Au and epithermal Au deposits: Products of remelting of subduction-modified lithosphere. Geology, 37(3), 247–250. doi: 10.1130/G25451A.1.

Richards JP. 2014. Porphyry and related deposits in subduction and post-subduction settings. Acta Geologica Sinica-English Edition, 88(s2), 535–537. doi: 10.1111/1755-6724.12374_19.

Richards JP. 2011. High Sr/Y arc magmas and porphyry Cu±Mo±Au deposits: Just add water. Economic Geology, 106(7), 1075–1081. doi: 10.2113/econgeo.106.7.1075.

Shafiei B, Haschke M, Shahabpour J. 2009. Recycling of orogenic arc crust triggers porphyry Cu mineralization in Kerman Cenozoic arc rocks, southeastern Iran. Mineralium Deposita, 44(3), 265–283. doi: 10.1007/s00126-008-0216-0.

Sillitoe RH. 2010. Porphyry copper systems. Economic geology, 105(1), 3–41. doi: 10.2113/gsecongeo.105.1.3.

Sui QL, Wang Q, Zhu DC, Zhao ZD, Chen Y, Santosh M, Hu ZC, Yuan HL, Mo XX. 2013. Compositional diversity of ca. 110 Ma magmatism in the northern Lhasa Terrane, Tibet: Implications for the magmatic origin and crustal growth in a continent-continent collision zone. Lithos, 168–169, 144–159. doi: 10.1016/j.lithos.2013.01.012.

Sun JD, Liu WC, Ren GS, Zhan LQ. 2018. Discussion on ore-forming material sources of Haobugao Pb-Zn deposit in Chifeng, Inner Mongolia. Advances in Geosciences, 8(8), 1330–1337 (in Chinese with English abstract). doi: 10.12677/AG.2018.88145.

Sun M, Tang JX, Chen W, Ma XD, Qu XM, Song Y, Li XY, Ding JS. 2020. Process of lithospheric delamination beneath the Lhasa-Qiangtang collision orogen: Constraints from the geochronology and geochemistry of Late Cretaceous volcanic rocks in the Lhasa terrane, central Tibet. Lithos, 105219, 356–357. doi: 10.1016/j.lithos.2019.105219.

Sun M, Tang JX, Chen W, Ma XD, Song Y, Zhang ZB, Liu QP. 2021. Timing and origin of the Shesuo skarn Cu-polymetallic deposit in the northern Lhasa subterrane, central Tibet: Implications for Early Cretaceous Cu (Mo) metallogenesis in the Bangong-Nujiang metallogenic belt. Ore Geology Reviews, 129, 103919. doi: 10.1016/j.oregeorev.2020.103919.

Tang JX, Yang HH, Song Y, Wang LQ, Liu ZB, Li BL, Lin B, Peng B, Wang GH, Zeng QG, Wang Q, Chen W, Wang N, Li ZJ, Li YB, Li YB, Li HF, Lei CY. 2021. The copper polymetallic deposits and resource potential in the Tibet Plateau. China Geology, 4(1), 1–16. doi: 10.31035/cg2021016.

Wan B, Deng C, Najafi A, Hezareh MR, Talebian M, Dong LL, Chen L, Xiao WJ. 2018. Fertilizing porphyry Cu deposits through deep crustal hot zone melting. Gondwana Research, 60, 179–185. doi: 10.1016/j.gr.2018.04.006.

Wang ZL, Fan JJ, Wang Q, Hu WL, Yang ZY, Wang J. 2021. Reworking of juvenile crust beneath the Bangong–Nujiang suture zone: Evidence from Late Cretaceous granite porphyries in Southern Qiangtang, Central Tibet. Lithos, 390–391, 106097. doi: 10.1016/j.lithos.2021.106097.

Wang W, Wang M, Zhai QG, Xie CM, Hu PY, Li C, Liu JH, Luo AB. 2020. Transition from oceanic subduction to continental collision recorded in the Bangong-Nujiang suture zone: Insights from Early Cretaceous magmatic rocks in the north-central Tibet. Gondwana Research, 78, 77–91. doi: 10.1016/j.gr.2019.09.008.

Wang Y, Ma XD, Qu XM, Chen W. 2019. Geochronology and petrogenesis of the Xiongmei Cu-bearing granodiorite porphyry in North Lhasa subterrane, central Tibet: Implication for the evolution of Bangong-Nujiang metallogenic belt. Ore Geology Reviews, 114, 103119. doi: 10.1016/j.oregeorev.2019.103119.

Wang Q, Tang JX, Chen YC, Hou JF, Li YB. 2019. The metallogenic model and prospecting direction for the Duolong super large copper (gold) district, Tibet. Acta Petrologica Sinica, 35(3), 879–896 (in Chinese with English abstract). doi: 10.18654/1000-0569/2019.03.16.

Wang Y, Tang JX, Wang LQ, Li S, Danzhen WX, Li Z, Zheng SL, Gao T. 2019. Magmatism and metallogenic mechanism of the Ga'erqiong and Galale Cu-Au deposits in the west central Lhasa subterrane, Tibet: Constraints from geochronology, geochemistry, and Sr-Nd-Pb-Hf isotopes. Ore Geology Reviews, 105, 616–635. doi: 10.1016/j.oregeorev.2019.01.015.

Wang Y, Ma XD, Chen W, Zeng YJ, Qu XM. 2018. The discovery of the tungsten mineralization in the middle part of the Bangonghu-Nujiang metallogenic belt and its significance. Mineral Deposits, 37(4), 885–888.

Wang Q, Zhu DC, Zhao ZD, Liu SA, Chung SL, Li SM, Liu D, Dai JG, Wang LQ, Mo XX. 2014. Origin of the ca. 90 Ma magnesia-rich volcanic rocks in SW Nyima, central Tibet: Products of lithospheric delamination beneath the Lhasa-Qiangtang collision zone. Lithos, 198–199, 24–37. doi: 10.1016/j.lithos.2014.03.019.

Wu H, Li C, Hu PY, Li XK. 2015a. Early Cretaceous (100–105 Ma) adakitic magmatism in the Dachagou area, northern Lhasa terrane, Tibet: implications for the Bangong-Nujiang Ocean subduction and slab break-off. International Geology Review, 57(9–10), 1172–1188. doi: 10.1080/00206814.2014.886152.

Wu H, Li C, Xu MJ, Li XK. 2015b. Early Cretaceous adakitic magmatism in the Dachagou area, northern Lhasa terrane, Tibet: implications for slab roll-back and subsequent slab break-off of the lithosphere of the Bangong-Nujiang Ocean. Journal of Asian Earth Sciences, 97, 51–66. doi: 10.1016/j.jseaes.2014.10.014.

Yazdi Z, Jafari Rad A, Aghazadeh M, Afzal P. 2019. Porphyry copper prospectivity mapping using fuzzy and fractal modeling in Sonajeel area, NW Iran. Bulletin of the Mineral Research and Exploration, 158, 235–250. doi: 10.19111/bulletinofmre.451565.

Yu SM, Ma XD, Song Y, Tang JX, Qu XM. 2020. Origin of Early Cretaceous Cu-bearing magmas associated with slab break-off in Northern Lhasa subterrane: Implications for the multisource of the postcollisional magma. Geological Journal, 55(6), 4642–4655. doi:

10.1002/gj.3659.

Yuan SD, Mao JW, Zhao PL, Yuan YB. 2018. Geochronology and petrogenesis of the Qibaoshan Cu-polymetallic deposit, northeastern Hunan Province: Implications for the metal source and metallogenic evolution of the intracontinental Qinhang Cu-polymetallic belt, South China. Lithos, 302–303, 519–534. doi: 10.1016/j.lithos.2018.01.017.

Zhao YY, Cui YB, Lv LN, Shi DH. 2011. Chronology, geochemical characteristics and the significance of Shesuo copper polymetallic deposit, Tibet. Acta Petrologica Sinica, 27(7), 2132–2142 (in Chinese with English abstract).

Zhao ZB, Li C, Ma XX. 2021. How does the elevation changing response to crustal thickening process in the central Tibetan Plateau since 120 Ma? China Geology, 4(1), 32–43. doi: 10.31035/cg2021013.

Yin A, Harrison TM. 2000. Geologic evolution of the Himalayan-Tibetan orogen. Annual Review of Earth and Planetary Sciences, 28(1), 211–280. doi: 10.1146/annurev.earth.28.1.211.

Zhu DC, Li SM, Cawood PA, Wang Q, Zhao ZD, Liu SA, Wang LQ. 2016. Assembly of the Lhasa and Qiangtang terranes in central Tibet by divergent double subduction. Lithos, 245, 7–17. doi: 10.1016/j.lithos.2015.06.023.

Zhu DC, Zhao ZD, Niu YL, Dilek Y, Hou ZQ, Mo XX. 2013. The origin and pre-Cenozoic evolution of the Tibetan Plateau. Gondwana Research, 23(4), 1429–1454. doi: 10.1016/j.gr.2012.02.002.

Zhu DC, Zhao ZD, Niu YL, Mo XX, Chung SL, Hou ZQ, Wang LQ, Wu FY. 2011. The Lhasa Terrane: Record of a microcontinent and its histories of drift and growth. Earth and Planetary Science Letters, 301(1–2), 241–255. doi: 10.1016/j.epsl.2010.11.005.

Zhu DC, Mo XX, Niu YL, Zhao ZD, Wang LQ, Liu YS, Wu FY. 2009. Geochemical investigation of Early Cretaceous igneous rocks along an east–west traverse throughout the central Lhasa Terrane, Tibet. Chemical Geology, 268(3–4), 298–312. doi: 10.1016/j.chemgeo.2009.09.008.

Zhu XS, Lu MJ, Cheng WJ, Song YC, Zhang C. 2017. Comparison of geological mineralogy and geochemical characteristics between ore-bearing porphyries of porphyry deposits in the Andean and the Gandise metallogenic belts. Geological Bulletin of China, 36(12), 2143–2153 (in Chinese with English abstract). doi: 10.3969/j.issn.1671-2552.2017.12.007.